Understanding the Role of Crystallographic Shear on the Electro-
chemical Behavior of Niobium Oxyfluorides

Journal:	*Journal of Materials Chemistry A*
Manuscript ID	TA-ART-02-2020-001406.R1
Article Type:	Paper
Date Submitted by the Author:	22-May-2020
Complete List of Authors:	Bashian, Nicholas; University of Southern California Preefer, Molleigh; University of California, Materials Research Laboratory Milam-Guerrero, Joanna; University of Southern California, Department of Chemistry Zak, Joshua; California Institute of Technology, Division of Chemistry and Chemical Engineering Ahsan, Suha; University of Southern California, Department of Chemistry Sendi, Charlotte; University of Southern California, Department of Chemistry Vincent, Rebecca; University of California, Materials Research Laboratory Haiges, Ralf; University of Southern California, Chemistry See, Kimberly; California Institute of Technology, Division of Chemistry and Chemical Engineering Seshadri, Ram; University of California, Materials Research Laboratory Melot, Brent; University of Southern California,

SCHOLARONE™
Manuscripts

Journal Name

ARTICLE TYPE

Understanding the Role of Crystallographic Shear on the Electrochemical Behavior of Niobium Oxyfluorides[†]

Nicholas H. Bashian,[a] Molleigh B. Preefer,[b] JoAnna Milam-Guerrero[a], Joshua J. Zak,[c] Charlotte Sendi,[a] Suha Ahsan,[a] Rebecca Vincent,[b] Ralf Haiges,[a], Kimberly A. See,[c] Ram Seshadri,[b] and Brent C. Melot[*d]

The effects of shear planes in perovskitic materials have been studied, in order to identify their role in the electrochemical behavior of Li^+ intercalation hosts. These planes modulate the structural stability and ionic transport pathways and therefore play an intimate role in the characteristics and performance of shear compounds. Herein, two Nb-based compounds, NbO_2F and Nb_3O_7F, were chosen as representative perovksite and shear derivatives respectively to investigate the role of crystallographic shear. A series of *operando* measurements, including X-ray diffraction and X-ray absorption spectroscopy, in conjunction with structural analysis, Raman spectroscopy, and detailed electrochemical studies identified the effect of shear planes. It was found that shear planes led to increased structural stability during Li^+ (de)intercalation with shear layers being maintained, while perovskitic layers were seen to degrade rapidly. However, disordering in the shear plane stacking introduced during delithiation ultimately led to poor capacity retention despite structural maintenance as Li^+ diffusion channels are disrupted.

1 Introduction

The structural distortions of lithium intercalation hosts have been an area of extensive research and are of the utmost importance to the design and operation of electrode materials for use in Li-ion batteries. The intercalation of Li^+ into a crystalline metal oxide framework and the associated redox often leads to destructive changes in bond lengths and a rearrangement of crystallographic building blocks, either by the distortion of existing chemical bonds or formation of new bonds, to accommodate inserted cations.[1] This dynamic process has a powerful influence on the electrochemical performance of battery electrode materials, affecting many aspects including capacity retention, polarization, and rate performance.[2,3] Many approaches have attempted to mitigate deleterious consequences of atomic rearrangement, in-cluding nanostructuring, architectural modification, and crystal structure engineering.[4–6]

Recently, niobium oxides based on perovskite and Wadsley-Roth phases have drawn increased interest for use in energy storage applications, due to a combination of high ionic and electronic conductivity which permits good rate performance, even in micron-sized particles.[7–9] First identified in the Ti-Nb-O phase space, Wadsley-Roth phases are formed by the removal of a plane of anions from the ReO_3 type structure resulting in alternating layers of edge sharing and corner sharing octahedral units.[10–15] Oxide shear phases have shown high rate performance in examples such as niobium-tungsten oxides and $TiNb_2O_7$ with some structures suppressing phase transformations during cycling, allowing for fast Li diffusion through the material.[16–19] A series of these compounds have been chemically or electrochemically lithiated, with studies suggesting the edge sharing shear planes stabilize the structure.[20–22]

Niobium based Wadsley-Roth shear phases represent a rich phase space, including Nb_3O_7F derived from the perovskite NbO_2F.[23] These formulas represent a ReO_3-type perovskite and a shear derivative of the form $3 \times \infty \times \infty$, respectively, with open channels allowing for ion insertion. We note the relatively uncommon one–dimensional structure type represents a shear plane along a single crystallographic axes, as opposed to the more common $m \times n \times \infty$ structure which forms two–dimensional $m \times n$ blocks.[24] The electrochemical behavior of per-

a Department of Chemistry, University of Southern California, Los Angeles, CA, 90089 USA.;
b Materials Research Laboratory, University of California, Santa Barbara, Santa Barbara, CA, 93106 USA.
c Division of Chemistry and Chemical Engineering, California Institute of Technology, Pasadena, California 91125, USA.
d Department of Chemistry, University of Southern California, Los Angeles, CA, 90089 USA.; E-mail: melot@usc.edu

Fig. 1 (a): NbO_2F exists in a perovskite structure with corner sharing octahedra. (b): Nb_3O_7F contains layers of edge sharing and corner sharing octahedra formed by the removal of an anionic plane of atoms from the perovskite structure. (c): Representative diagram of the shear relationship between NbO_2F and Nb_3O_7F.

ovskite and perovskite-derived phases has been investigated in the past, with studies showing the reversible electrochemical cycling of both NbO_2F and Nb_3O_7F.[25–28] Additionally, structural analogues based on $TiOF_2$ and VO_2F compositions have been shown to cycle Li^+ reversibly.[29,30]

Our group has previously investigated the electrochemical (de)lithiation of the archetypical perovskite, ReO_3, using *operando* X-ray diffraction (XRD) measurements to characterize a correlated rotation of ReO_6 polyhedra upon lithiation.[31] It was postulated by Cava *et al.* that a shear structure of ReO_3 would make this twisting motion more difficult due to the inclusion of edge-sharing octahedra.[32] The identification of structural characteristics that control such phase changes is of inherent importance to the design of next generation lithium ion battery electrodes. As such, we began a study to determine the effects of shear structuring on the electrochemical performance of niobium oxyfluorides.

As both Cava and Permér observed, the formation of crystallographic shear planes affects structural changes caused by Li-insertion reactions into perovskites by limiting the rotational freedom of octahedral units.[22,33,34] Due to the expected differences in ion mobility and structural stability, the electrochemical behavior of these materials is of great interest. Therefore, we began a series of *operando* XRD and X-ray absorption (XAS) measurements in conjunction with detailed electrochemical characterization and Raman spectroscopy to illustrate the effect of shear planes in the niobium oxyfluorides, NbO_2F and Nb_3O_7F, identifying multiple regions throughout the (de)lithiation process where the inclusion of shear planes was manifested.

2 Experimental Methods

CAUTION: Anhydrous HF and associated reagents can cause severe chemical burns. Before undertaking any experiments, one should familiarize oneself with the hazards associated with all reagents as well as proper handling and techniques. Fresh tubes of calcium gluconate gel should be available for fast treatment of skin exposure by any reagents. For additional information, please see Segal *et al.*[35]

2.0.0.1 Synthetic Methods. NbO_2F particles, of several hundred nanometers in diameter, were prepared using an adaptation of the method reported by Frevel *et al.*[36] Large batches of NbO_2F were prepared by dissolving Nb_2O_5, as purchased, in anhydrous HF in a fluorinated ethylene propylene (FEP) tube in a liquid nitrogen bath. The reaction was slowly brought to room temperature while being stirred and the excess HF was removed by vacuum to yield $NbO_2F \cdot HF$ salt. Due to the hygroscopic nature of the salt, it was stored in an inert atmosphere. The complexed HF was removed from the salt by heating under vacuum at 150°C for a period of 12 hours to yield NbO_2F as a pale lavender powder.

Nb_3O_7F was prepared by grinding Nb_2O_5 with polytetrafluoroethylene (PTFE) in a 1 : 3 molar ratio and pressing into a pellet followed by heating in a quartz glass ampule sealed under vacuum. Heating was performed in a Panasonic 1200 W microwave set to 60% power for a period of 13 minutes, with the glass ampule contained in a bed of charcoal to act as a microwave susceptor.

2.0.0.2 Physical Characterization. Laboratory XRD patterns were collected on a Bruker D8 diffractometer with a Cu K_α source (λ_1 = 1.5406 Å, λ_2 = 1.5444 Å), equipped with a Lynxeye XE-T detector. High resolution synchrotron powder diffraction data was collected using beamline 11-BM at the Advanced Photon Source (APS), Argonne National Laboratory using an average wavelength of 0.45784 Å. Discrete detectors covering an angular range from -6 to 16° 2θ were scanned over a 34° 2θ range, with data points collected every 0.001° 2θ and scan speed of 0.01°/s. The resulting diffraction patterns were refined against published structures using the Rietveld method as implemented in the Full-Prof program.[36–39] Scanning Electron Microscopy (SEM) was conducted on a FEI Nova Nano 650 FEG SEM. NbO_2F was analyzed at 10 kV; Nb_3O_7F was analyzed at 5 kV. The particles were uncoated and measurements were made in immersion mode.

2.0.0.3 Electrochemical Characterization. The electrochemical performance of both materials was characterized using Swagelok-type cells assembled in an argon-filled glovebox, using Li metal as a combined counter and reference electrode and Whatman GF/D borosilicate glass fiber sheets as the separator. 1 M $LiPF_6$ in ethylene carbonate and dimethylcarbonate (1:1 v/v) was used as the electrolyte (LP30). Thick film electrodes prepared by blending 10% graphite powder (300 mesh), 10% acetylene black, 20% polytetraflouroethylene (average particle size of 1 μm), and 60% active material, and pressing under a hydrostatic pressure of 0.9 tons to yield electrodes of 10-15 mg (total). Given the insulating nature of the active material, the chosen electrode formulation ensured adequate electrical conductivity. Cell components and electrodes of both NbO_2F and Nb_3O_7F were dried under vacuum at 110°C before assembly

2.0.0.4 *Operando* Measurements. *Operando* X-ray Absorption Spectroscopy (XAS) measurements were performed at beamline 12-BM, APS using the AMPIX electrochemical cell, equipped
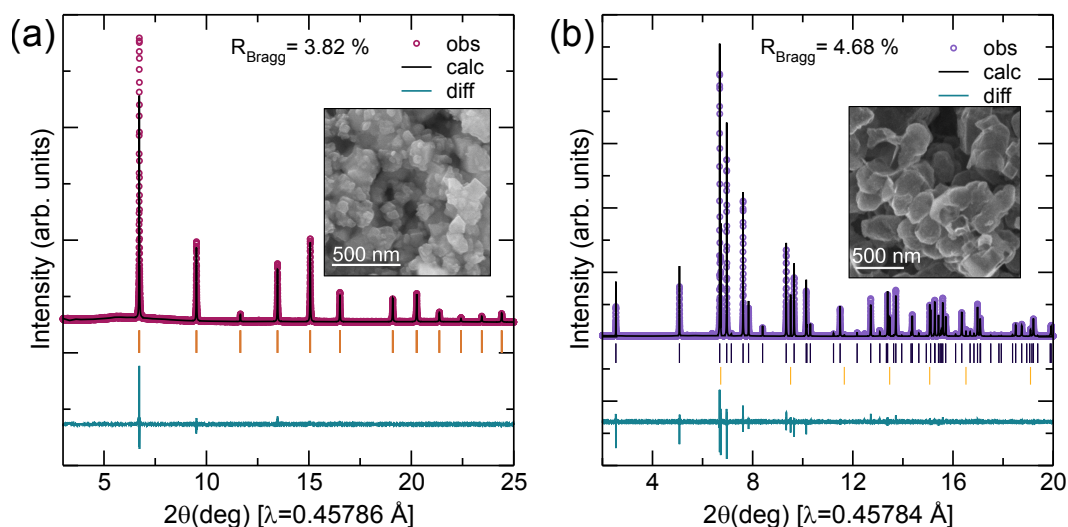
Fig. 2 Rietveld refinement of synchrotron XRD data of NbO_2F (a) showed phase pure product while refinement of Nb_3O_7F (b) revealed a small impurity of less than 1% NbO_2F, illustrated by the orange reflections. Both compounds have small particle sizes, as shown in SEM imaging (insets).

with a glass fiber separator and a Li foil combined counter and reference electrode. Methods were adopted from Borkiewicz et al. [40] XAS measurements were performed in transmission geometry at the Nb K-edge (18.9 KeV), using Nb foil as a reference. Scans were collected in transmission mode over a span of eight minutes. XAS data processing was carried out using the ATHENA software of the package IFEFFIT. [41] The EXAFS component was normalized and converted to wavenumber. The resultant signal in k-space was multiplied by k^3, Fourier-transformed and left with no phase shift correction. All displayed EXAFS data is shown with no phase shift correction. *Ab initio* calculations on relevant structure models were done using the code FEFF8.2 with fits being performed using the ARTEMIS software of the IFEFFIT package. [41,42]

Operando XRD measurements were performed using a Bruker D8 diffractometer with a Cu K_α source (λ_1 = 1.5406 Å, λ_2 = 1.5444 Å), equipped with a Lynxeye XE-T detector. A modified Swagelok cell, with Be window serving as a current collector, allowed for diffraction patterns to be collected during electrochemical cycling. XRD scans were performed in a Bragg-Brentano geometry over a range of 20° to 50° 2θ for NbO_2F and 15° to 50° 2θ for Nb_3O_7F with a total scan time of 20 minutes. Scans were continuously repeated throughout the duration of electrochemical cycling. The same thick film electrodes, glass fiber separators, LP30 electrolyte, and Li foil counter electrodes previously described were used for cell preparation.

2.0.0.5 Raman Spectroscopy. Electrochemical cells of both NbO_2F and Nb_3O_7F were prepared as described above. Cells were discharged at a rate of $C/10$ based on one electron per formula unit. Cells were disassembled in an Ar-filled glovebox and the working electrodes were washed with dimethylcarbonate and dried under active vacuum overnight. Raman spectra were collected on a Horiba XploRA One confocal Raman microscope. All spectra were collected with a 532 nm diode laser, a diffraction grating with groove density 2400 g mm^{-1}, and laser power ranging from 1.6-8 mW. The hole and slit were fixed at 500 and 50 μm, respectively. The laser was focused using a 50× (numeri-

cal aperature 0.5) objective, which yielded a spot size of *ca.* 1.3 μm. An acquisition time of 3 s was used, and 100 spectra were accumulated and averaged.

3 Experimental Results

Several forms of niobium oxyfluorides are known and present an opportunity to investigate the effects of structural changes on the electrochemical behavior of the redox active niobium, in conjunction with the effects of fluorination. NbO_2F crystallizes in the prototypical perovskite structure in space group Pm$\bar{3}$m (#221), with corner sharing NbO_4F_2 octahedra arranged in an ordered network with Nb–O–Nb bond angles of 180°, as shown in Figure 1(a). [36] The vacant A-site in the structure creates three–dimensional channels for ion intercalation. In order to reduce the probability of residual HF or hydroxyl moieties from remaining in the NbO_2F, we employed anhydrous HF and *in vacuo* heatings during synthesis. Based on analysis of synchrotron XRD there is less than one percent impurities present in the sample, however even a minute Nb^{4+} impurity could lead to the slight lavender coloring in the sample.

Nb_3O_7F crystallizes in space group Cmmm (#65), as shown in Figure 1(b), and is formed by a shearing of the octahedral layers of NbO_2F which creates alternating sheets of edge sharing and corning sharing Nb octahedra in an ABAB stacking pattern. A representative diagram of the shearing motion is displayed in Figure 1(c). The edge sharing octahedra are slightly distorted due to repulsion, resulting in a long and a short Nb–O bond along the a-axis, while the four bonds in the b–c plane are found to be equivalent.

Both the symmetry and purity of NbO_2F and Nb_3O_7F were confirmed through Rietveld refinement of synchrotron XRD data, as shown in Figure 2(a) and (b) respectively, with refinement parameters provided in S.I. Table T1[†]. Given the very similar X-ray cross sections of oxygen and fluorine, no evidence of fluorine ordering can be seen in Rietveld refinements on either compound. As demonstrated in the inset of Figure 2(a), SEM imaging

of NbO_2F reveals cubic particles on the order of $100-200$ nm in diameter. Small particles were expected given the low temperature synthetic methods employed. Similarly, the extremely short heating time used in the synthesis of Nb_3O_7F was expected to create small particle size and SEM images confirmed particles of $150-300$ nm (Figure 2(b) inset). The use of microwave techniques in the synthesis yielded smaller particle sizes than previously reported methods.
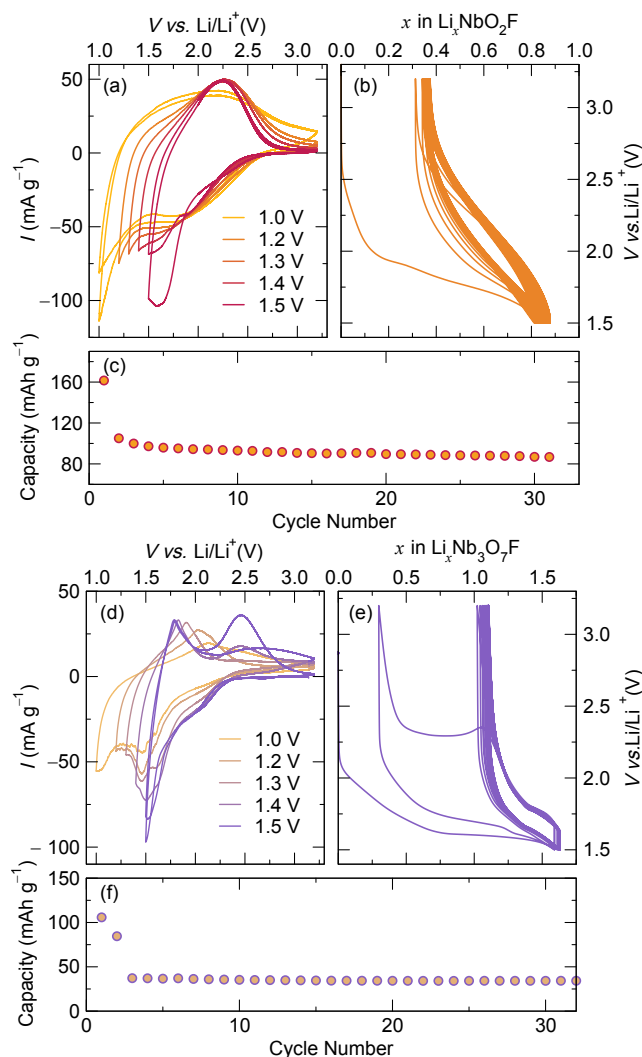
Fig. 3 (a): Cyclic voltammetry with a gradually expanding window illustrate the effects of structural change on the electrochemical cycling of NbO_2F. Lower voltage limits of each trace are provided in the legend while all traces used an upper voltage limit of 3.2 V. (b): Galvanostatic cycling of Li_xNbO_2F in the voltage window of $1.5-2.0$ V shows cycling on the $Nb^{5+/4+}$ redox couple with good reversibility. (c) Capacity of each cycle shows stable behavior after the initial cycle. In (d), a window opening CV experiment on Nb_3O_7F showed that the oxidative peak at 2.5 V is lost as the reductive limit is lowered, with lower voltages in the legend. In (e) galvanostatic cycling of Nb_3O_7F at a C/10 rate shows substantial irreversible capacity followed by stable solid solution cycling. In (f) the capacity retention is shown over 30 cycles.

The (de)lithiation of both NbO_2F and Nb_3O_7F was probed through various methods including galvanostatic cycling and cyclic voltammetry, with several key behavioral differences identi-

fied in the following sections. The cycling behavior of NbO_2F was investigated through cyclic voltammetry (CV) measurements that provided precise identification of redox voltages and details on the intercalation process. A voltage window opening experiment, in which the lower limit of a CV was lowered in a stepwise fashion, was used to identify the coupling of different redox processes in correlation with structural changes. Figure 3(a) demonstrates two different regions present, most clearly seen by examining the window from $1.5-3.2$ V in comparison with the window from $1.0-3.2$ V. The first window shows a relatively sharp redox couple centered around 1.9 V; from galvanostatic measurements, it was seen that this region demonstrates better reversibility. This is contrasted by the latter window, in which the redox peaks are seen to become extremely broad with the oxidative wave stretching from 1.3 V to 2.8 V, indicative of disordering introduced in the structure that leads to a range of site energies for (de)intercalation and a poorly defined redox potential. This structural disorder is induced throughout the window opening, as shown by the gradually broadening redox peaks as the voltage window is widened and the 3+ oxidation state of Nb is reached. A CV experiment over a wide voltage window of $1.0-3.2$ V (S.I. Figure S3) was used to confirm that the broadening was not a function of extended cycling, as a very broad oxidative peak was seen on the first charge cycle.

Galvanostatic cycling over a wide voltage window of $1.0-3.2$ showed that it was possible to insert two full units of Li^+ in NbO_2F, with corresponding reduction of Nb^{5+} to Nb^{3+}, however this reaction was found to be mostly irreversible and the cells rapidly lost capacity, as shown in S.I. Figure S1[†]. However, analysis of the derivative curve (inset of S.I. Figure S1[†]) indicated multiple reaction redox events occurring with an initial reduction seen between $1.5-2.0$ V, followed by a subsequent broad reduction below 1.5 V. In an effort to improve reversible cycling, NbO_2F was cycled with a higher lower voltage cutoff, as shown in Figure 3(b). It was found that a cutoff voltage of 1.5 V led to improved cycling stability in these compounds, with a reversible capacity of approximately 90 mAh/g after 30 cycles, as shown in 3(c), suggesting that to Nb^{3+} is irreversible.

In an effort to understand the role of structural shear planes in modifying electrochemical behavior, cyclic voltammetry was performed on Nb_3O_7F revealing an evolution in behavior during extended cycling that suggests structural changes were induced due to lithiation. Figure 3(a) shows that the redox behavior of Nb_3O_7F changes as the lower voltage limit is shifted downwards, leading to the loss of an oxidative peak at 2.5 V and the sharpening of a peak at 1.75 V. In the first cycles of the CV, from $1.5-3.2$ V, two distinct oxidation peaks are seen. We note the presence of a distinct peak at 2.5 V, reminiscent of the oxidative peak observed in NbO_2F cycled over the same voltage window. However, lowering of the voltage window leads to a loss of intensity and a gradual shifting of the two oxidative peaks, possibly reflecting structural changes in the material. This suggests that structurally distinct lithiation sites in the perovskitic layers of the shear structure are lost upon greater reduction of the structure, possibly due to an inability of the corner sharing Nb octahedra to accommodate changes in bond distance induced by a lowered oxidation
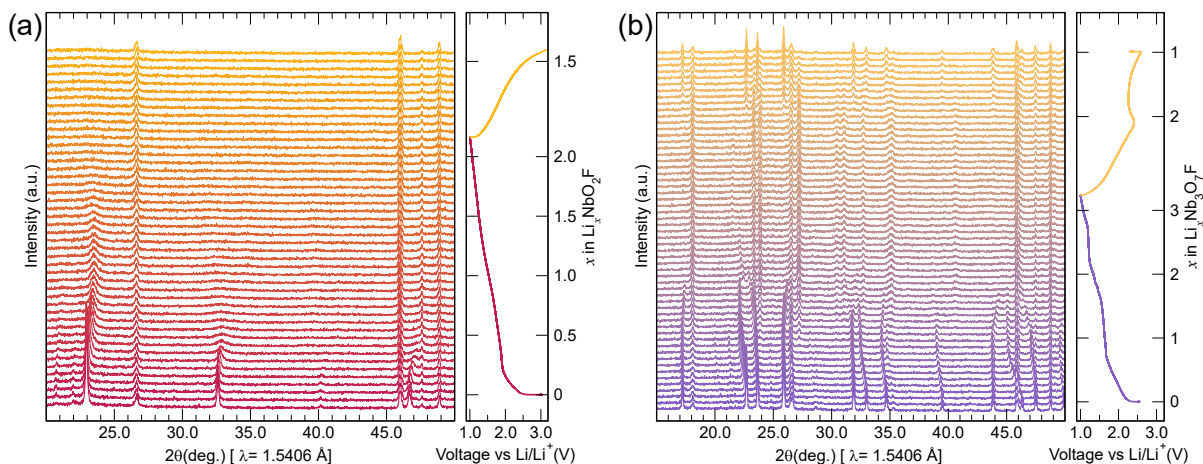
Fig. 4 *Operando* XRD measurements of NbO_2F (a) throughout a complete discharge/charge cycle reveals the loss of crystallinity induced by lithiation to Li_2NbO_2F. The loss of intensity on diffraction peaks is not recovered upon charging. In comparison, the structure of Nb_3O_7F (b) is seen to go through multiple changes during lithiation followed by a complete recovery upon charging, albeit with lowered crystallinity.

state.

Further evidence of this change in structure is seen in S.I. Figure S4[†] which shows multiple CV cycles of Nb_3O_7F over the voltage window $1.0 - 3.2$ V. The oxidative peak at 2.5 V is shifted upwards by 0.25 V on the first cycle, with this larger polarization reflecting the increased energy necessary to remove Li^+ from the structure. This peak is maintained for only the first two cycles, while the redox couple centered at 1.75 V is seen to cycle with relatively good stability for many cycles, suggesting better structural stability for lithiation at a structurally distinct site We observe that deep discharge to 1.0 V leads to a rapid changes in redox behavior with the loss of the higher voltage oxidative peak, likely due to greater structural rearrangement.

Galvanostatic cycling of Nb_3O_7F from $1.0 - 3.2$ V shows a large irreversible capacity on the initial cycle associated with the oxidative plateau observed at 2.5 V eventually being replaced with stable solid solution type cycling, which results in a reversible capacity of approximately 85 mAh/g, as shown in S.I. Figure S2[†]. During the charging process, the voltage trace dips downwards at approximately 2.5 V before continuing to rise sharply, implying an overall lowering of the structural energy of the $Li_xNb_3O_7F$ after partial delithiation. In an effort to improve the reversibility of cycling Nb_3O_7F a voltage window of $1.5 - 3.2$ V was used, as shown in Figure 3(b). Interestingly, we found that the voltage dip observed in S.I. Figure S2[†] was also present when a higher voltage limit was used; however, the feature did not reappear on subsequent cycles. Instead multiple charge/discharge cycles led to a smooth, featureless voltage curve with no apparent plateaus.

As will be demonstrated in subsequent sections, the drop in voltage observed during the charge curve is associated with structural changes that occur as shear layers in the structure rotate about one another. An analysis of *operando* XRD patterns provides an excellent visualization of the structural changes induced by lithiation of both NbO_2F and Nb_3O_7F. During the initial lithiation of NbO_2F, diffraction peaks shift steadily to higher angles as shown in Figure 4(a). This peak shifting observed is likely associated with a rotation of the octahedral subunits that comprise

the structure as the unit cell shrinks during lithiation to stabilize Li^+ ions in vacancies within the structure. Due to the entirely corner sharing structure in NbO_2F, contraction can occur only by rotation or distortion of the octahedral units with precedent for octahedral rotation.[31] The upwards peak shift is followed by a substantial decrease in peak intensity at greater degrees of lithiation as crystallinity and long-range order are lost. The loss of crystallinity is further visualized in a heatmap of diffracted intensity as a function of state of charge in S.I. Figure S5[†].

As Li^+ is cycled in NbO_2F, the bond lengths change to accommodate redox activity which causes changes in bond lengths and a flexing of the unit cell. Similar behavior has been observed in the isostructural ReO_3, where the contraction and expansion of the unit cell led to fracturing of particles.[31] While reduction of NbO_2F by two units of lithium leads to a mostly amorphous material and loss of nearly all crystallinity, cycling of a single Li^+ with a cutoff voltage of 1.5 V allows for better structural maintenance. As shown in S.I. Figure S6[†], during two discharge/charge cycles of NbO_2F with a lower voltage limit of 1.5 V, diffraction peaks are maintained and a corresponding expansion of the unit cell on delithiation is observed, suggesting that the structure can accommodate $Nb^{5+/4+}$ redox but accesing $Nb^{4+/3+}$ redox leads to an irreversible transformation. During the insertion of one Li^+, the main structural peaks of NbO_2F shift to higher angles indicating a contracting unit cell, while this process is reversed upon deinsertion. The smaller bond distance changes and reduced strain necessitated by the single redox event allows the structure NbO_2F to be maintained.

An interesting contrast is drawn upon examination of the electrochemical and structural evolution of Nb_3O_7F during lithiation, in which the presence of shear planes could provide a stabilizing force, allowing for greater structural maintenance throughout electrochemical (de)lithiation. In Figure 4(b), it is seen that lithiation of Nb_3O_7F causes large changes in the diffraction pattern, with an initial expansion of the unit cell in the *a-b* plane, for example along the (1 1 0) peak at 23.5°. Upon further lithiation, the loss of starting peaks and introduction of additional peaks is ob-

served, but interestingly, the peaks that are retained in the XRD pattern are primarily associated with shear layers. These shear layer peaks, corresponding to reflections such as the (3 1 0) or (1 1 0) at 26.4° and 23.5° respectively, are seen to shift and split thus indicating the potential lowering of the space group. This is indeed the case as the peaks are matched from an orthorhombic to triclinic unit cell where the triclinic phase is present at lithium values of $x = 1.71$ upon discharge to $x = 1.96$ upon charge (S.I. Figures S7 and S8[†]). This value is consistent with data from chemical lithiation by Permér *et al.*, albeit electrochemical lithiation affords a more gentle lithiation process thereby allowing the structure to accommodate more lithium before undergoing a phase transition to a lower symmetry space group.[34]

The gradual XRD peak shift on discharge is indicative of a solid solution process; the charging process occurs through phase growth in which the starting structure is recovered (S.I. Figures S7 and S9[†]). The phase growth occurs in the same region where the oxidative voltage dip was noted in Figure 3(b) and S2. These differences between discharge and charge suggest that the lithiation process disrupts the perovskitic linkage between shear planes, leading to a loss of peak intensity with diffraction planes containing those layers. Upon charging, the stabilized shear layers allow the structure to partially reform, however stacking faults occur in the layers, ultimately affecting electrochemical performance.

While XRD measurements provided insight into average structural changes, *operando* XAS measurements were used to monitor the Nb oxidation state as well as local structural changes during cycling. All distances discussed and the displayed data are not phase shifted. As shown in S.I. Figure S10[†], the Nb K-edge was tracked throughout a complete discharge cycle of NbO_2F to Li_2NbO_2F, which results in the reduction of Nb^{5+} to Nb^{3+}. This causes a downshift in the K-edge energy that shifts steadily with lithiation and restructures in shape due to structural rearrangement. The radial distribution function, generated from the Fourier transform of the XAS data, provides a depiction of local structural changes, as shown in Figure 5(a). During initial lithiation, the second-shell peak at 3.5 Å is seen to steadily lose intensity while shifting to longer distances. Fits of the EXAFS data show that this peak is primarily composed of Nb–Nb scattering distances between octahedra. As NbO_2F is lithiated over one unit of Li^+, the Nb octahedral linkage is disrupted resulting in a loss of a coherent scattering distance.

Further *operando* XAS measurements were performed on the Nb K-edge in Nb_3O_7F throughout a complete discharge/charge cycle in order to probe the reaction mechanism. As expected, the Nb K-edge is observed to shift to lower energies throughout lithiation, followed by reversal upon delithiation, with this process visualized in S.I. Figure S11[†]. An incomplete recovery of the K-edge is indicative of the partial irreversibility of the reaction, as Nb is not fully oxidized back to the +5 oxidation state. This indicates the partial irreversibility associated with lithiation. Additionally, the radial distribution shows changes throughout the cycling of Nb_3O_7F, as shown in Figure 5(b). As Nb_3O_7F is lithiated, a peak at 3.4 Å is seen to lower in intensity, eventually disappearing completely in the fully discharged material. However, this peak is
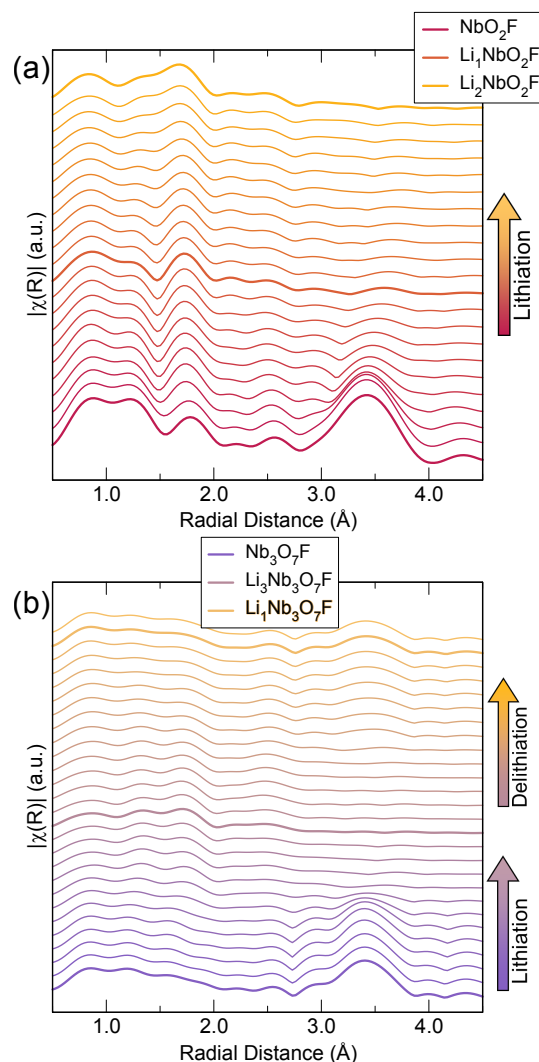
Fig. 5 (a): The radial distribution function indicates substantial local rearrangement around Nb atoms in NbO_2F, with a loss of a peak at 3.4 Å. (c) The radial distribution function of Nb_3O_7F, seen throughout a complete (de)lithiation cycle. Note the loss and eventual partial return of the peak at 3.4 Å.

partially recovered upon charging, as some intensity is seen at 3.4 Å in the fully charged material. This peak corresponds the Nb-Nb distances in the perovskitic layers of the Nb_3O_7F structure, which are disrupted during lithiation but may be partially recovered after delithiation. Interestingly, this peak does not shift upwards during lithiation as is seen in the peak at 3.4 Å in NbO_2F.

To further probe changes to the structure of NbO_2F and Nb_3O_7F upon lithiation, *ex situ* Raman spectroscopy was measured on samples discharged to 1.5 V and 1 V. The spectra for the NbO_2F compound along with the reduced NbO_2F are shown in Figure 6(a). The full wavenumber range can be found in S.I. Figure S12. The pristine NbO_2F spectrum contains several broad vibrational modes that are assigned in S.I. Table T2. The most notable modes are the intense mode centered at 703 cm^{-1} and the shoulder at 620 cm^{-1}, which are assigned to the NbO_6 symmetric stretch and bridging Nb-O-Nb stretch, respectively.[43] Upon reduction to 1.5 V, both modes lose intensity and new, strong

modes appear at 597 cm^{-1} and 816 cm^{-1}, which suggests a significant change in the crystal symmetry around the NbO$_6$ octahedra and their linkages. Further evidence for significant symmetry changes is found in the low wavenumber region of the spectrum. The broad modes in pristine NbO$_2$F yield to much more defined, sharp modes in the sample discharged to 1.5 V. The new modes are interestingly similar to those in the low wavenumber region of the pristine Nb$_3$O$_7$F. Upon further reduction to 1 V, the new mode at approx. 597 cm^{-1} is maintained but the 816 cm^{-1} disappears again suggesting significant structural changes. The Raman spectrum of NbO$_2$F after reduction does not maintain any features found in the spectrum of the pristine material other than a mode at 620 cm^{-1} related to the corner-sharing connectivity of the octahedra. The loss of the mode at 703 cm^{-1} coupled with the sharpening of modes at lower wavenumbers shows a significant change in local symmetry upon reduction. The changes are large enough to disturb the long-range order, as observed by the loss in diffraction intensity in the *operando* XRD.

The Raman spectra of Nb$_3$O$_7$F and the reduced compounds are shown in Figure 6(b). The modes observed in the pristine material are assigned in S.I. Table T3. The Raman spectrum of the pristine Nb$_3$O$_7$F has two modes in the region between 500 and 800 cm^{-1}, similar to those in NbO$_2$F. The mode at approx. 703 cm^{-1} is similarly attributed to the NbO$_6$ symmetric stretch.[44] The shoulder at 620 cm^{-1} is again associated with the bridging Nb-O-Nb stretch, however, the mode is sharper compared to the 620 cm^{-1} mode in NbO$_2$F which could be due to the increased rigidity introduced to the structure by the shear planes in Nb$_3$O$_7$F.[44] Similarly, the low wavenumber modes are much sharper than those in NbO$_2$F indicating less disorder and decreased flexibility due to the restrictions imposed by the added shear plane. Upon reduction to 1.5 V, the modes associated with NbO$_6$ octahedra and the Nb-O-Nb stretch are largely maintained in addition to the low wavenumber modes. The lack of change between the two vibrational spectra suggest that reduction does little to affect the local symmetry.

Upon discharging to 1 V, the spectrum maintains a broad mode around 620 cm^{-1} that is red shifted from the pristine material suggesting that the NbO$_6$ octahedra are maintained, but the reduced Nb causes a relaxing of the modes. Interestingly, the sharp mode around 620 cm^{-1} in the pristine and the discharged to 1.5 V material either disappears or broadens significantly. As the 620 cm^{-1} mode is related to the Nb-O-Nb stretch of the corner sharing octahedra, it is unlikely that the mode would disappear and instead we suggest that it is broadening. Furthermore, larger changes are observed in the mode at 703 cm^{-1} upon discharge of Nb$_3$O$_7$F to 1 V, which is when the triclininc phase is seen to form in *operando* XRD. We note that there is also a very sharp mode at 128 cm^{-1} in the Nb$_3$O$_7$F that blue shifts upon reduction to 1.5 V and red shifts after reduction to 1 V. The assignment of the mode is unknown, however, and so we do not consider this mode further.

4   Discussion

A derivative of NbO$_2$F, Nb$_3$O$_7$F presents an interesting comparison on the effects of bonding by introducing a shear plane of
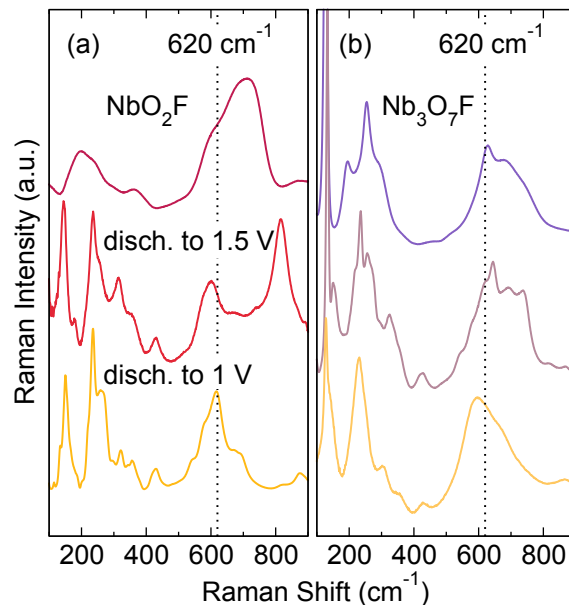
Fig. 6 (a): The Raman spectra of pristine NbO$_2$F as well as NbO$_2$F discharged to 1.5 V and 1.0 V, shows the disappearance of several modes followed by the introduction of new modes. (b) The Raman spectra of Nb$_3$O$_7$F, at various points of discharge, shows better maintenance of the modes seen in the pristine Nb$_3$O$_7$F.

edge-sharing NbO$_4$F$_2$ rock salt layers separated by corner sharing octahedra. The crystal structures of NbO$_2$F and Nb$_3$O$_7$F were first characterized by Frevel and Andersson, respectively, whom undertook studies on the synthesis and thermal stability of these compounds.[36,39,45,46] It was found that Nb$_3$O$_7$F could be synthesized by the decomposition of NbO$_2$F, illustrating the formation of a shear plane by the collapse of a perovskite layer.[46] The close relation between the phases was further examined by Permér and Lundberg, who investigated the chemical lithiation of NbO$_2$F and Nb$_3$O$_7$F and their relationship.[33,34,47] The chemical lithiation of NbO$_2$F was seen to cause a distortion of the cubic structure to the hexagonal phase, LiNbO$_3$ at higher states of lithiation.[33] We observe greatly improved cycling stability in NbO$_2$F when the lower voltage cutoff was limited to 1.5 V preventing the formation of Nb^{3+}. Given the contraction of the unit cell seen during *operando* XRD, it is likely that the structure is unable to accommodate the change in bond length necessitated by Nb^{3+}, and the large unit cell volume changes result in cracking of particles and electrical isolation that leads to poor reversibility. Therefore, it is advantageous to cycle in a higher voltage regime, avoiding the formation of Nb^{3+}.

Shear planes have been observed to stabilize perovskite structures by limiting distortion, leading to excellent electrochemical cycling stability by resisting cracking during unit cell volume change. The shear plane blocks have been shown to suppress rotational motion.[48] As first observed by Cava *et al.*, the structure of Nb$_3$O$_7$F does not contain orthogonal shear planes nor the associated structural blocks, such as those found in TiNb$_2$O$_7$.[22] This was postulated to allow for a twisting motion between sheets to accommodate lithiation; however this flexibility ultimately leads to poor reversibility in cycling due to incomplete structural recov-

ery. Further detail can be derived from chemical lithiation experiments, in which Nb_3O_7F was found to be relatively stable, maintaining symmetry until $Li_{1.2}Nb_3O_7F$, followed by a collapse of the structure to hexagonal $LiNbO_3$. Chemical delithiation was shown to reform Nb_3O_7F, albeit with the inclusion of stacking faults, resulting in greater disorder.[34] A collapse of the corner sharing layers by stacking faults would create a much denser structure, hindering lithium movement and suppressing cycling. The edge sharing layers effectively close a channel in the structure, affecting ion movement through the lattice, while also reducing the crystallographic sites available for lithiation.[22]

It is likely that Nb_3O_7F forms mainly edge sharing planes after the first cycle, which further decrease Li^+ channels and result in the loss of capacity observed. Both electrochemical measurements and XRD results show that Nb_3O_7F is nucleated after the first charge, likely with an increase in shear layers. The one–dimensional shear planes only interrupt slip planes in a single direction whereas other shear shear structure types interrupt rotation in multiple directions.

Additional evidence of rotational disorder is observed in the Raman spectra of Nb_3O_7F by tracking the broadening of the mode at 620 cm^{-1}. A broadening of the mode indicates a broader dispersity of the vibrations, reminiscent of the mode observed in pristine NbO_2F. Thus, we suggest that the broadening is due to a loss of structural rigidity upon reduction which would suggest that the shear planes are not sufficient to stabilize the structure at 1 V. However, it is important to note that the vibrational spectrum of the reduced Nb_3O_7F maintains many of the features in the pristine material with some broadening suggesting that, at least compared to NbO_2F, the Nb_3O_7F structure is more stable during reduction.

5   Conclusions

Through a series of electrochemical and structural studies, we have identified the role of octahedral rotations in destabilizing perovskitic and shear derivative structures towards ion (de)intercalation. In the perovskite NbO_2F, a contraction of the unit cell, facilitated by twisting of octahedral polyhedra, is induced by reductive Li^+ insertion eventually, leading to a loss of structural coherence. In order to prevent the destabilization and densification of the material, the Nb^{3+} oxidation state must be avoided, as this state causes an unsustainable amount of strain to be accommodated within the structure.

Meanwhile, the shear structure Nb_3O_7F is seen to be more stable during Li^+ insertion, as the more rigid edge–sharing shear planes are less susceptible to twisting and cracking, leading to the shear planes being maintained during cycling. However, the unique $3 \times \infty \times \infty$ shear structure, where shear planes extend along a single crystallographic direction, allows for movement of the edge sharing sheets as the perovskitic linkages twist and contract during lithiation, similar to what was seen in NbO_2F. Upon delithiation, mismatch and stacking faults between the shear layers leads to poor cycleability as ion diffusion pathways are closed and Li^+ sites are lost.

Hence, we conclude that although the structure of Nb_3O_7F is slightly stabilized by shear planes, the one-dimensional shear

planes are still subject to large degrees of rotational motion. Thus, we suggest that shear planes in orthogonal directions are required to suppress the movement of layers relative to one another. This study provides a valuable design principle for the use of crystallographic shear as a mechanism to stabilize intercalation electrode materials.

Conflicts of interest

The authors declare no conflicts of interest.

Acknowledgements

Notes and references

1 S. M. Whittingham, *Intercalation Chemistry (Materials science and technology)*, Academic Press, 1982.

2 D. R. Sadoway and A. M. Mayes, *MRS Bulletin*, 2002, **27**, 590–596.

3 C. Julien, A. Mauger, K. Zaghib and H. Groult, *Inorganics*, 2014, **2**, 132–154.

4 K. Kang, *Science*, 2006, **311**, 977–980.

5 T. Brezesinski, J. Wang, J. Polleux, B. Dunn and S. H. Tolbert, *J. Am. Chem. Soc.*, 2009, **131**, 1802–1809.

6 T. Brezesinski, J. Wang, S. H. Tolbert and B. Dunn, *Nat. Mater.*, 2010, **9**, 146–151.

7 Q. Cheng, J. Liang, Y. Zhu, L. Si, C. Guo and Y. Qian, *J. Mater. Chem. A*, 2014, **2**, 17258–17262.

8 K. J. Griffith, K. M. Wiaderek, G. Cibin, L. E. Marbella and C. P. Grey, *Nature*, 2018, **559**, 556–563.

9 K. J. Griffith, A. C. Forse, J. M. Griffin and C. P. Grey, *J. Am. Chem. Soc.*, 2016, **138**, 8888–8899.

10 A. D. Wadsley, *Acta Crystallogr.*, 1961, **14**, 660–664.

11 A. D. Wadsley, *Acta Crystallogr.*, 1961, **14**, 664–670.

12 R. S. Roth and A. D. Wadsley, *Acta Crystallogr.*, 1965, **18**, 724–730.

13 J. S. Anderson, *Reactions in Crystallographic Shear Structures*, Elsevier, 1982, pp. 503–538.

14 L. A. Bursill and B. G. Hyde, *Philos. Mag.*, 1971, **23**, 3–15.

15 L. A. Bursill, B. G. Hyde and D. K. Philp, *Philos. Mag.*, 1971, **23**, 1501–1513.

16 K. J. Griffith, I. D. Seymour, M. A. Hope, M. M. Butala, L. K. Lamontagne, M. B. Preefer, C. P. Koçer, G. Henkelman, A. J. Morris, M. J. Cliffe, S. E. Dutton and C. P. Grey, *J. Am. Chem. Soc.*, 2019, **141**, 16706–16725.

17 C. P. Koçer, K. J. Griffith, C. P. Grey and A. J. Morris, *J. Am. Chem. Soc.*, 2019, **141**, 15121–15134.

18 J. W. Kim, V. Augustyn and B. Dunn, *Adv. Energy Mater.*, 2011, **2**, 141–148.

19 V. Augustyn, J. Come, M. A. Lowe, J. W. Kim, P.-L. Taberna, S. H. Tolbert, H. D. Abruña, P. Simon and B. Dunn, *Nat. Mater.*, 2013, **12**, 518–522.

20 D. W. Murphy and P. A. Christian, *Science*, 1979, **205**, 651–656.

21 D. W. Murphy, M. Greenblatt, R. J. Cava and S. M. Zahurak, *Solid State Ionics*, 1981, **5**, 327–329.

22 R. J. Cava, *J. Electrochem. Soc.*, 1983, **130**, 2345.

23 S. Cordier, T. Roisnel and M. Poulain, *J. Solid State Chem.*, 2004, **177**, 3119–3126.

24 S. Andersson, *Bull. la Soc. Fr. Mineral. Cristallogr.*, 1967, **90**, 522–527.

25 C. Bohnke, O. Bohnke and J. L. Fourquet, *Mol. Cryst. Liq. Cryst.*, 1998, **311**, 23–29.

26 C. Bohnke, J. L. Fourquet, N. Randrianantoandro, T. Brousse and O. Crosnier, *J. Solid State Electrochem.*, 2001, **5**, 1–7.

27 M. Reddy, S. Madhavi, G. S. Rao and B. Chowdari, *J. Power Sources*, 2006, **162**, 1312–1321.

28 D. Saritha, *Mechanics, Materials Science & Engineering*, 2018, **14**, 1–6.

29 N. Louvain, Z. Karkar, M. El-Ghozzi, P. Bonnet, K. Guérin and P. Willmann, *J. Mater. Chem. A*, 2014, **2**, 15308–15315.

30 J. C. Pérez-Flores, R. Villamor, D. Ávila-Brande, J. M. G. Amores, E. Morán, A. Kuhn and F. García-Alvarado, *J. Mater. Chem. A*, 2015, **3**, 20508–20515.

31 N. H. Bashian, S. Zhou, M. Zuba, A. M. Ganose, J. W. Stiles, A. Ee, D. S. Ashby, D. O. Scanlon, L. F. J. Piper, B. Dunn and B. C. Melot, *ACS Energy Lett.*, 2018, **3**, 2513–2519.

32 R. Cava, A. Santoro, D. Murphy, S. Zahurak and R. Roth, *J. Solid State Chem.*, 1982, **42**, 251–262.

33 L. Permér and M. Lundberg, *J. Solid State Chem.*, 1989, **81**, 21–29.

34 L. Permér, *J. Solid State Chem.*, 1992, **97**, 105–114.

35 E. B. Segal, *Chem. Health Saf.*, 2000, **7**, 18–23.

36 L. K. Frevel and H. W. Rinn, *Acta Crystallogr.*, 1956, **9**, 626–627.

37 H. M. Rietveld, *J. Appl. Crystallogr.*, 1969, **2**, 65–71.

38 J. Rodriguez-Carvajal, *IUCr Newsl.*, 2001, **26**, 1.

39 S. Andersson, S. Åsbrink, T. Reistad and D. R. Sparrow, *Acta Chem. Scand.*, 1964, **18**, 2339–2344.

40 O. J. Borkiewicz, B. Shyam, K. M. Wiaderek, C. Kurtz, P. J. Chupas and K. W. Chapman, *J. Appl. Crystallogr.*, 2012, **45**, 1261–1269.

41 B. Ravel and M. Newville, *J. Synchrotron Radiat.*, 2005, **12**, 537–541.

42 A. L. Ankudinov, B. Ravel, J. J. Rehr and S. D. Conradson, *Phys. Rev. B*, 1998, **58**, 7565–7576.

43 H. Ullah, K. Guerin and P. Bonnet, *Eur. J. Inorg. Chem.*, 2019, **2019**, 230–236.

44 F. Idrees, C. Cao, F. K. Butt, M. Tahir, M. Tanveer, I. Aslam, Z. Ali, T. Mahmood and J. Hou, *CrystEngComm*, 2013, **15**, 8146.

45 S. Andersson, A. Åström and B. C. L. Weedon, *Acta Chem. Scand.*, 1964, **18**, 2233–2236.

46 S. Andersson, A. Åström, C. Issidorides and A. Kallner, *Acta Chem. Scand.*, 1965, **19**, 2136–2138.

47 L. Permér and M. Lundberg, *J. Less Common Met.*, 1989, **156**, 145–159.

48 H. Yu, J. Zhang, R. Zheng, T. Liu, N. Peng, Y. Yuan, Y. Liu, J. Shu and Z.-B. Wang, *Mater. Chem. Front.*, 2020, 1.